Selective characterization of petroporphyrins in shipping fuels and their corresponding emissions using electron-transfer matrix-assisted laser desorption/ionization Fourier transform ion cyclotron resonance mass spectrometry

Maxime Sueur, Christopher Rüger, Julien Maillard, Hélène Lavanant, Ralf Zimmermann, Carlos Afonso

Selective characterization of petroporphyrins in shipping fuels and their corresponding emissions using electron-transfer matrix-assisted laser desorption/ionization Fourier transform ion cyclotron resonance mass spectrometry

Maxime SUEUR[1,2], Christopher P. RÜGER*[2,3,4], Julien F. MAILLARD[1,2], Hélène LAVANANT[1], Ralf ZIMMERMANN[3,4], Carlos AFONSO[1,2]

[1]Normandie Université, COBRA, UMR 6014 et FR 3038, Université de Rouen, INSA de Rouen-Normandie, CNRS, IRCOF, Mont Saint Aignan Cedex

[2]International Joint Laboratory - iC2MC: Complex Matrices Molecular Characterization, TRTG, BP 27, 76700 Harfleur, France.

[3]Joint Mass Spectrometry Centre/Chair of Analytical Chemistry, University of Rostock, 18059 Rostock, Germany.

[4]Department Life, Light & Matter (LLM), University of Rostock, 18051 Rostock, Germany

*** corresponding author:** christopher.rueger@uni-rostock.de

DOI 10.1016/j.fuel.2022.126283

Received 15 April 2022; Received in revised form 1 October 2022; Accepted 8 October 2022

Graphical Abstract

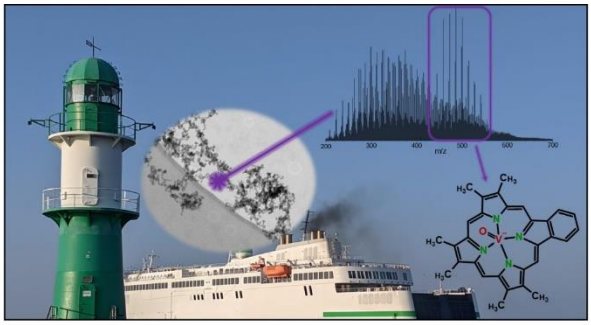

Abstract

In the context of the global transportation of goods, shipping emissions account for a significant proportion of air pollution. Indeed, a focus has been made over recent years on this primary emission source, leading to several regulations with respect to the chemical composition of shipping fuels. However, these regulations mainly concern the fuel sulfur content (FSC) and do not consider other compound classes such as polycyclic aromatic hydrocarbons (PAHs) or metal-containing aromatics, i.e., petroporphyrins, known to be present in bunker fuels. Petroporphyrins are tetrapyrrole-based metal complexes derived from the transformation of chlorophylls through geological time scales. In contrast to PAHs, their fate in the combustion process and effects on environmental health are widely unknown. In this study, we present electron-transfer ionization in matrix-assisted laser desorption/ionization Fourier transform ion cyclotron resonance mass spectrometry (ET-MALDI FTICR MS) for the characterization of vanadyl and nickel porphyrins in shipping feed fuels and primary particulate matter emissions. For the first time, these petroporphyrins could successfully be described in the heavy fuel oil (HFO) feeds but also in the particles emitted by the combustion of the respective fuel on a molecular level. Three main alkylated series of porphyrins were observed; these series can be qualified by their double bond equivalent, i.e. 17, 18, and 20, and correspond to various core structures. Our results highlight the molecular fate of the petroporphyrins through combustion and show that a significant amount of petroporphyrins is released unburned or partially dealkylated to the atmosphere. Furthermore, our results suggest that a higher amount of petroporphyrins might be released in harbors than in open sea, due to a less efficient combustion at lower engine load. This last observation motivates a future specific study on porphyrins' health and environmental effects.

1. Introduction

Among the various sources of anthropogenic emissions, shipping is one of the largest contributors to the total emissions of the transportation sector. In 2007, Corbett et al. estimated that shipping emissions accounted globally for 60,000 cardiopulmonary and lung cancer deaths annually under the regulation at that time. Most of those deaths can be related to major trade routes such as European and southwest Asian coastlines.[1] Furthermore, other health effects can be associated to shipping emissions via oxidative stress and inflammation.[2] Aside from the environmental health aspects, shipping emissions have a direct impact on climate, depending on their intrinsic radiative forcing. For example, black carbon (BC)[3], CO_2 and O_3 have a positive radiative forcing (RF) as opposed to sulfate particles which have a negative RF. Organic aerosols also induce indirect effects on climate by modifying the optical properties of clouds, causing a negative RF. This indirect effect is estimated to outweigh the greenhouse gas warming effect, leading to a negative net RF from the shipping emissions.[4] Shipping emissions exhibit a unique molecular profile, different from other sources, such as biomass burning or road engine emissions.[5] In 2020, a novel regulation limiting the sulfur content in shipping fuels from 3.5% (m/m) to 0.5% (m/m) by International Marine Organization (IMO) became effective [6]. This regulation is even more restrictive in Sulfur Emission Control Areas (SECAs), where fuel-sulfur content (FSC) has been limited to 0.1% (m/m) since 2015[6]. The aim of this restriction was to decrease the sulfur content of the shipping emissions either by causing a switch from classical bunker or heavy fuel oils (HFO) towards cleaner feed fuel alternatives such as marine gas oil (MGO) or by using exhaust gas after-treatment (scrubber technology) to wash the emissions.[7] Compared to MGO, HFO emissions exhibit a particular toxic mixture with higher concentrations of particulate matter (PM), polycyclic aromatic hydrocarbons (PAH), heavy alkanes and metals, such as nickel and vanadium.[8-13] However, combustion of the cleaner distillate fuel MGO emits higher levels of soot, which is a known carcinogen, and induces strong toxicological effects.[14] Furthermore, most organic species in the aerosol are transferred directly from the fuel as unburnt material, especially at lower power operations.[15] Vanadium and nickel in HFO are mostly present as oxides. However, approximately 10% are present as organometallic compounds such as petroporphyrins.[16, 17] Petroporphyrins are tetrapyrrole-based metal complexes.[18] They are the results of chlorophylls' degradation over geological time through diagenesis and catagenesis processes[19]. The molecular fate of these porphyrins after combustion in a ship engine is largely unknown. Furthermore, even though, health and environmental effects of heavy metals such as nickel and vanadium are studied [20, 21], the ecological impact of organic species containing such metals is largely unknown.

Bunker fuels and their corresponding combustion engine emissions are highly complex mixtures composed of numerous organic and inorganic species. This chemical complexity requires state-of-the-art instrumentation for molecular-level analysis. Examples of such instrumentation, specifically deployed towards shipping emissions, involve chromatographic separations like gas chromatography selective ion monitoring mass spectrometry (GC-SIM-MS) [22], or , high resolution time of flight mass spectrometry (HR-ToF-MS) coupled to two-dimensional gas chromatography (GC×GC). Other use direct introduction or other means of sample introduction and ionization like thermal-desorption of needle trap devices coupled to photoionization time-of-flight mass spectrometry (NTD-TD-REMPI-ToF-MS) [23], direct

inlet probe (DIP) or thermogravimetric analysis (TGA)[24], proton transfer reaction mass spectrometer (PTR-MS)[25]. Finally, high resolution-time of flight-aerosol mass spectrometry (HR-ToF-AMS) [26], consists in HR-ToF-MS coupled to a sampling, separating and ionizing unit allowing real time analysis of aerosols [27]. Nonetheless, despite the existence of established technologies in aerosol science, none of these techniques was able to attribute metalorganic residues in carbonaceous aerosols on a molecular level. Another technique that has been used for the in-depth characterization of shipping fuels and their emissions is the laser desorption/ionization Fourier transform ion cyclotron resonance mass spectrometry (LDI-FTICR-MS) [28], which promotes the ionization of aromatic and polycyclic aromatic compounds. In this respect, targeting petroporphyrins, with their aromatic functionalities, in particulate matter by LDI might be suitable [29, 30]. LDI time-of-flight mass spectrometry has been used in literature for the characterization of petroporphyrins from various petroleum matrices [29, 31]. Particularly, the Kilpatrick group contributed methods for petroporphyrin purification and molecular analysis [30, 32].

However, direct LDI may cause fragmentation of labile analytes such as the petroporphyrins, potentially cleaving off alkylation side-chains or altering the aromatic backbone.[33] Electron-transfer matrix-assisted laser desorption/ionization (ET-MALDI) has been shown to circumvent this drawback for the specific compound class of petroporphyrins [31]. In brief, ET matrices allow the ionization of analytes based on their ionization energy (IE): if the matrix' IE is higher than the analyte's IE, its ionization can occur through charge exchange processes,[34] and vanadium and nickel porphyrins exhibit a distinctly low IE (6.5-7.5 eV). [33] Derivated cyano-phenylenevinylenes (CNPV) has been reported as an efficient matrix for selective ionization of petroporphyrins in crude oil, and especially the α-cyanophenylenevinylene derivative (α-CNPV-CH_3, IE=8.42 eV) recently developed and introduced by Ramirez-Pradilla et al.[33-35] Other ionization techniques are able to detect petroporphyrins, such as atmospheric pressure photoionization (APPI)[36, 37] and positive-ion electrospray ionization-(ESI+) using sodium attachment instead of proton or electron transfer as an ionization channel[38]. Bunker fuel emissions are highly complex, thus high mass accuracy and ultrahigh resolution of the FTICR MS are required to distinguish the targeted petroporphyrins from other molecular classes.

The scope of this study is the characterization of the petroporphyrins in different bunker fuels and the respective emissions obtained after their combustion in a ship diesel engine by ET-MALDI FTICR MS. Indeed, we chose ET-MALDI to address these metalorganic constituents not only in petrochemical feed fuels but also in the linked combustion emissions. This work focuses on tracing the fate of petroporphyrins in the combustion process by comparing the fuels and their corresponding emissions. We aimed at tracing dealkylation processes, oxidation, or other reactions that occur prior to the thermal decomposition of these metalorganic targets in the engine into smaller products, ultimately to metal oxides, NO_x, CO_2, and water. For this purpose, feed and emissions of HFOs with different FSC were studied, and of a porphyrin-free MGO, which was used as a control. To the best of the authors' knowledge, this is the first method aiming at the analysis of petroporphyrins on the molecular level in an environmental aerosol sample. This molecular knowledge should help to understand shipping emissions more in detail and especially the, for now, somewhat unknown and poorly described petroporphyrins fraction.

2.Experimental section

2.1. Fuel samples characteristics and preparation. Four fuels used for shipping with different chemical properties were investigated (Table 1). The heavy fuel oils (HFO) differ in their sulfur contents. Among the four fuels, only the marine gas oil (MGO) and the heavy fuel oil A (HFO A), have a sulfur content less than or equal to 0.5% (m/m), meeting the sulfur requirement from the International Marine Organization [6]. 1 mg of each fuel was diluted in 2 mL of HPLC grade (99.9%) acetonitrile (ACN, CAS: 75-05-8) and put in an ultrasonic bath for 10 min. The ACN was then completely evaporated using a N_2 stream and the samples were diluted in 2 mL of extra pure (99.9%) tetrahydrofuran (THF, CAS: 109-99-9). Furthermore, we also made a blank sample without using fuel to have a control sample.

Table 1: Sulfur, vanadium and nickel mass fraction of the fuels.

Fuel	Sulfur content (%)	Vanadium content (ppm)	Nickel content (ppm)
MGO	0.0015	<1	<1
HFO A	0.53	26	20
HFO B	1.02	57	<1
HFO C	2.16	237	23

2.2. Aerosol samples characteristics and preparation. PM was obtained through the combustion of the above-mentioned fuels in a one-stroke 80 kW research ship diesel engine operating at four different power loads during a measurement campaign at the University of Rostock (Germany) in 2020 (Table 2). See Table S 1 for engine details. This engine ran at the four power loads following the ISO 8178-4 E2 norm, i.e. 24 min at 100%, 60 min at 75% and 18 min at 50 and 25% as described by Streibel et al. for a previous campaign [13, 15]. The particulate matter was sampled on pre-baked and cleaned quartz fiber filters (QFF) at specific operating points and subjected to an elemental analysis by an in-situ inductively coupled plasma (ICP). For the analysis referred herein, 1/8 of each QFF was extracted in 1.5 mL of ACN and mixed in an ultrasonic bath for 10 minutes. The extract was then filtered on 0.2 µm PTFE membrane filter using a syringe filter holder and dried under a N_2 flow until the ACN evaporated. Finally, the dry extracts were dissolved in 50µL of ACN. Furthermore, the extraction step was also performed on a blank filter to obtain a control sample.

Table 2: Mass of vanadium and nickel quantified on the filter depending on the fuel and power load of the engine.

Sample name	Fuel used	Load (kW)	Vanadium amount on the filter (µg)	Nickel amount on the filter (µg)
PM A	HFO A	20 (25%)	1.37	0.70
PM B	HFO B	20 (25%)	0.73	0.54
PM C	HFO C	20 (25%)	7.39	1.95
PM C′	HFO C	60 (75%)	9.89	2.43

The α-cyanophenylenevynylene ET-matrix (α-CNPV-CH_3) was synthesized as previously reported [33] and dissolved in THF to reach a concentration of 1mg/mL.

2.3. Mass spectrometry. Mass spectra were acquired using a Bruker solarix XR 12T (Paracell™) instrument, equipped with a MALDI source (3.5

mbar) using a Nd:YAG×3 solid-state laser (355nm) in positive mode. The laser was used under the following conditions: focus 40.4%; frequency 2 kHz; number of shots per scan: 100. Different laser power settings were tested within a range of 14 to 30% and found to be optimal at 20% for LDI experiments on fuel extracts, and 15 % or 17 % for ET-MALDI experiments on fuel and particles extracts, respectively (Figure S 1 in the supplementary information) [39]. 200 transients were acquired and added up. Each transient was digitalized using 4M data points and a mass range ranging from *m/z* 110 to 1100, resulting in a transient duration of 1.26 s. The time of flight for trapping ions in the ICR cell was set to 1 ms. For LDI-FTICR experiments, 7 µL of each fuel extract were deposited on the MALDI target. For the MALDI FTICR experiments, 2 µL of matrix solution were mixed with 5 µL of fuel extract and 5 µL of matrix were mixed with 2 µL of particle extract prior to deposition on the MALDI target. More matrix solution had to be used for the study of particle extract because, as shown later, porphyrin signals relative intensity is much lower in the particles than in the fuel. Therefore it required a higher quantity of matrix to enhance porphyrins ionization and to be able to identify the porphyrins among the other signals of particle extracts. For each analysis, triplicate measurements were collected on a same sample.

2.4. Porphyrins attributions. Raw spectra were treated with Data Analysis 5.0 (Bruker Daltonics, Bremen, Germany). Internal calibration was performed using already known $C_xH_yN_1$ and C_xH_y molecular series and $C_xH_yN_4VO$ species identified in HFO C (termed N_1, CH, and N_4VO). The internal calibration list is given in supporting information (See Table S 2). A preliminary porphyrins attribution was performed using the SmartFormula tool from DataAnalysis. To focus on metal-containing ions, the molecular attribution boundaries were set as follow: $C_xH_yN_4VO_{1-3}S_{0-1}$ for vanadyl porphyrins and $C_xH_yN_4Ni$ for nickel porphyrins; with a minimal double bond equivalent [40] (DBE) of 17 , a minimum signal-to-noise ratio of 4 and a maximum mass error of 0.5 ppm. More flexible limits were also used to detect any chemical transformation through combustion of the porphyrins, i.e. lower DBE boundary, higher oxygen number (up to 7) and lower number of nitrogen (down to 2). Then, the peak list was also subjected to a Kendrick mass defect analysis [41, 42] using a self-written python 3.7.11 routine to extract each of alkylated porphyrin series , i.e. porphyrins with the same DBE, directly from the mass list. Details on this procedure are given in the supporting information and illustrated on Fig S 2. Within a series, any missing porphyrin were searched manually with DataAnalysis and their isotopic pattern was checked. Several molecular attributions of porphyrins therefore slightly exceeded the maximum error or had a low relative intensity and signal-to-noise ratio. Self-written python routines were used for plotting and data visualization.

3.Results and discussion

3.1. Effect of the ET-matrix on fuel and particle samples. Prior to the in-depth characterization of the porphyrins, the effects and suitability of the ET-matrix was investigated. The main interest of this type of matrix is to hinder the ionization of species having a higher ionization energy (above 8.42 eV) in favor of species having a lower ionization energy, such as PAHs with large conjugated π electron systems or petroporphyrins with their electro-excessive pyrrole cycles. Indeed, the ionization energy (IE) of the α-CNPV-CH3 matrix is higher than the one of the petroporphyrins; this difference of IE, superior to a 0.5 eV gap[43], allows for electron

transfer reactions to occur as described in equation (1) and (2) where m is the matrix and A the analyte.

$m + hv \rightarrow m^{+\bullet} + e^{-}$ (1)

$m^{+\bullet} + A \rightarrow m + A^{+\bullet}$ (2)

The isobaric complexity confirmed the need to use a FTICR MS platform to be able to resolve the peaks of interest among the multitude of signals originating from the sample and matrix signals. In fact, the mass difference between a vanadyl petroporphyrins such as $C_{28}H_{28}N_4OV$ and the $C_{36}H_{23}O_2$ from the $C_xH_yO_2$ oxygenated series present within both fuel and PM mass spectra is below 0.5 mDa. On the LDI mass spectrum of HFO C (Figure 1a), the main distribution centered around *m/z* 350. Classically, it corresponds to the apolar species ionized by laser desorption, i.e., homologue alkylated series of the CH, S_1 S_2, N_1 and N_2 classes. Another distribution around *m/z* 500 corresponded to the porphyrins' region. In each enlargement, attributed vanadyl porphyrins with a DBE of 17 are marked with a red dot and those with DBE 18 with a blue dot. In the shipping feed fuel sample, the effect of the matrix addition is already easily noticeable in the broadband visualization (insets in figure 1) as the addition of the matrix caused the distribution around *m/z* 500 to appear. The signals corresponding to the vanadyl porphyrins series were significantly more intense in the ET-MALDI mass spectrum of the fuel sample (Figure 1b) than in the LDI mass spectrum of the same fuel sample (Figure 1a), to the point of becoming the most intense peaks of the mass spectrum. In the LDI mass spectrum of the PM sample (Figures 1c), a low-intensity distribution centered around *m/z* 350 could be detected but no porphyrins were evidenced. However, on the ET-MALDI mass spectrum of the PM sample (Figures 1d), the distribution around *m/z* 500 could clearly be distinguished and several signals could be attributed to porphyrins. In fact, the chosen α-CNPV-CH3 matrix was able to significantly enhance the detection of petroporphyrins in both fuel and PM samples. Such enhancement of detection of petroporphyrins, thanks to the selective ionization of low IE molecules, first evidenced in heavy residues, crude oils and asphaltenes[33, 35] from fossil origin could therefore be successfully transferred here to the analysis of environmental PM samples. In the case of the primary ship emission PM, the drastic increase in ionization response by addition of the ET matrix allowed to overcome the low concentrations and made a detection feasible. All following experiments were thereafter performed with the ET matrix to ensure an efficient characterization of petroporphyrins and to compare the petroporphyrin content between feed fuel and PM emission. In addition to the previously characterized fuel samples, marine gas oil (MGO), a light fuel used in freight transport, was analyzed but no petroporphyrins were found, as seen in Figure S 4.

3.2. Preliminary characterization of petroporphyrins. The tetrapyrrole core of the petroporphyrins can chelate various metallic elements such as vanadium, nickel, iron, manganese, or copper[18]. Vanadyl and nickel porphyrins are the only types of petroporphyrins detected in the studied samples. However, even with the ET matrix, no petroporphyrins were detected in the PM A, which resulted from the combustion of the HFO A. Moreover, no nickel porphyrins were evidenced in the Particles B sample.

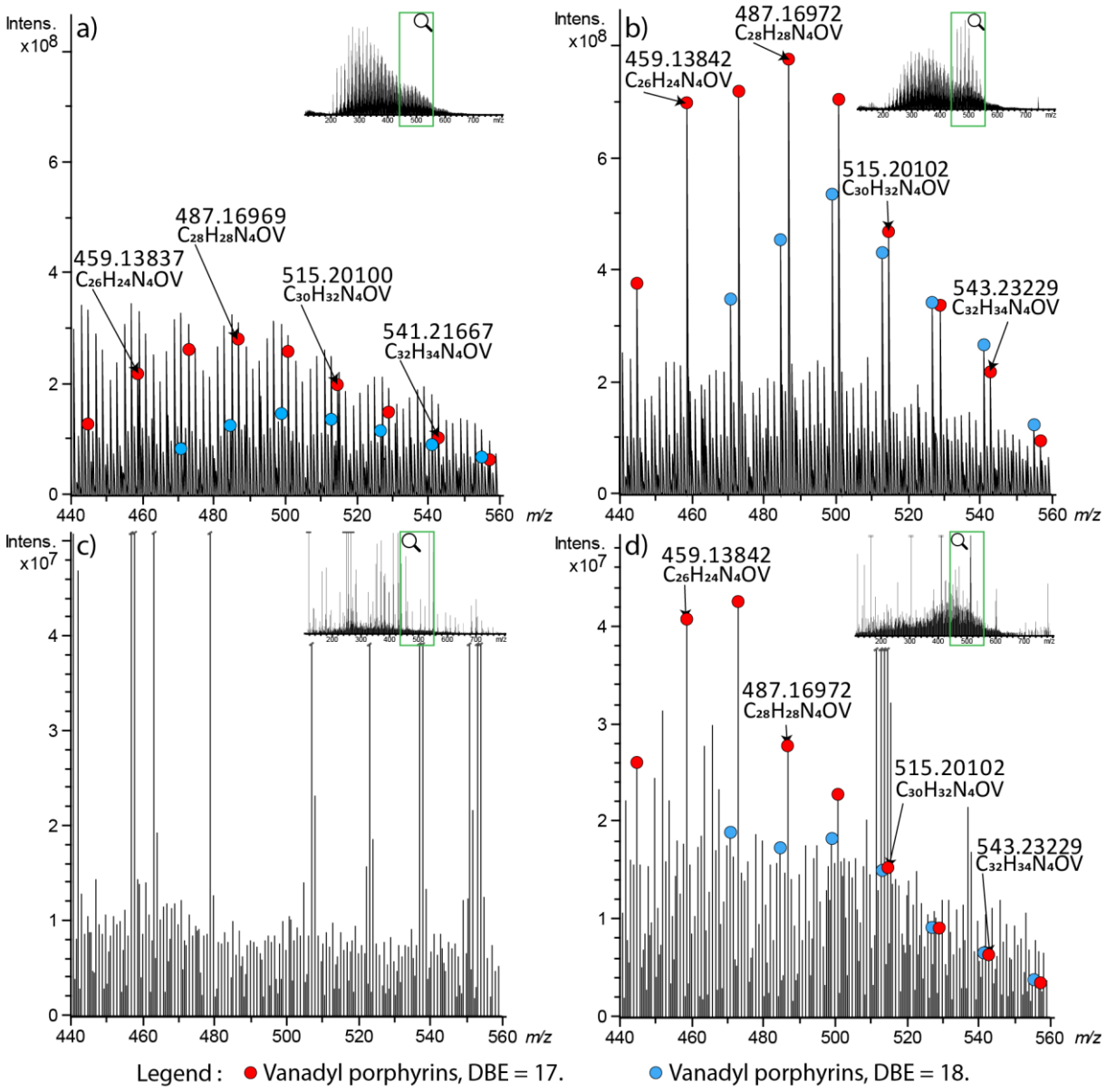

Figure 1: Broadband and zoomed mass spectra presenting the influence of the ET-Matrix in the petroporphyrins range of mass to charge ratio. The occurrence of selected petroporphyrin series is given as red (vanadyl, DBE 17) and blue (vanadyl, DBE 18) marks. a): HFO C; b): HFO C with matrix; c)PM C; d): PM C with matrix. No porphyrin species were detected in the PM sample without ET matrix.

As a preliminary rough comparison between the fuels and their corresponding emissions, the intensity of vanadyl and nickel porphyrins signals relative to the summed intensity of attributed species in the mass spectra are displayed in Figure 2. We found the relative intensity of petroporphyrins signals were significantly higher in the HFO C than in the other fuels. A student's t test[44] at a confidence level of 95%, performed thanks to the triplicates measurements, confirmed this observation, as shown on Figure 2 and found in Table S 3. The same observations were made with PM C with respect to PM B and PM A. This was consistent with the high vanadium and nickel contents in the corresponding feed fuel C (Table 1). Elemental analysis was used to determine vanadium and nickel contents, but such analyses does not provide information on the chemical

speciation of the elements, i.e., either mineral inorganic state or complexed metalorganic condition in porphyrin cores. In fact, in fossil material, a high fraction of vanadium and nickel content are included in porphyrin cores[17, 45]. Notably, we observed a decrease of the relative intensity of porphyrin signals between the HFO A and HFO B sample, which is not the tendency described by the above-mentioned elemental analysis (Table 1). In fact, the vanadium content in HFO B was twice that of HFO A, suggesting that an important fraction of vanadium and nickel in HFO B actually correspond to a mineral inorganic state, which couldn't be detected using ET-MALDI.

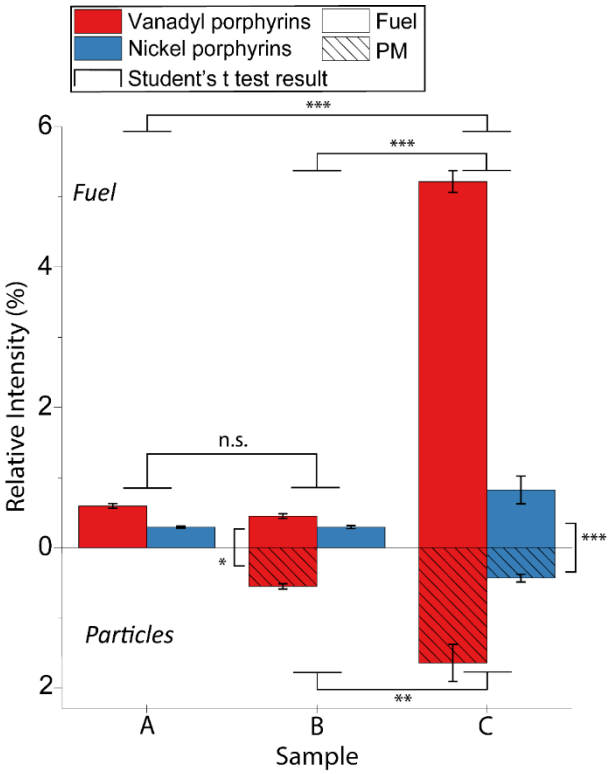

*Figure 2: Comparison between vanadyl and nickel petroporphyrins intensities. Results of Student's t test (CL = 95%) showing if a difference is statistically significant or not[44] : n.s.: non-significant with a confidence level of 95%, */**/***: significant with p-value respectively below 0.05, 0.01 and 0.001.*

Finally, the relative intensity of porphyrins is lower in the particles samples than in the feed fuels, hinting at their consumption through combustion. Due to their higher intensity vanadyl porphyrins are more easily detectable and thus characterizable than nickel porphyrins in the studied samples.

Figure 3 presents the distribution of the relative intensity of petroporphyrins according to their double bond equivalent (DBE). Interestingly, all samples exhibited the same DBE pattern: etio petroporphyrins were the most intense, followed by rhodo and rhodo-etio porphyrins[19, 46] (Figure 4). On the one hand, this finding lets us hypothesize that these three specific petroporphyrins are the most abundant in the different heavy fuel oils, regardless of their sulfur, vanadium or nickel content. Similar DBE distributions were obtained before and after combustion. A Pearson correlation of the DBE distribution shape between fuel samples and their corresponding emissions confirmed this similarity. The correlation coefficient between HFO C/Particles C and HFO B/Particles B were above 0.95 (0.9771 and 0. 9568, respectively), leading to α-values under the maximum acceptable value (α=0.05) for a confidence level of 95%. The results of these correlations and details on the applied procedure can be found in supporting information (Table S 4). As the combustion process did not affect the DBE pattern, we inferred the combustion did not single out any specific structure. Indeed, the DBE is a relevant indirect measure to the common petroporphyrin's structure is it allows to discriminate plausible core structures. According to the literature, the most plausible core structures for DBE 17, 18 and 20 petroporphyrins are etio-, DPEP-(deoxophylloerythroetio porphyrin) and rhodo-etio- cores, respectively[47, 48] (Figure 4).

The global maximum DBE observed was 27 in the HFO C; even though only an almost negligible number of signals corresponds to this DBE value,

this limit was consistent with the maximum DBE observed by Ramirez-Pradilla et al.[35] in 2019 in crude oil samples using the same matrix. Furthermore, we did not observe any petroporphyrins under the DBE 17, neither in the fuel nor in the PM, which would have hinted at ring opening through the combustion process.

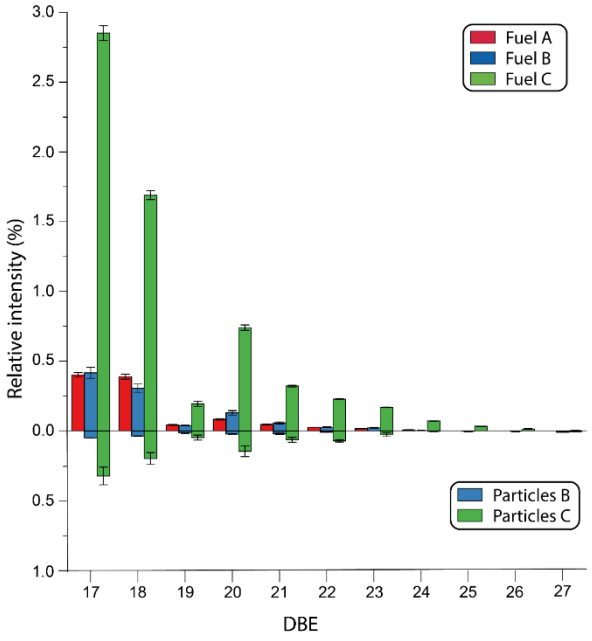

Figure 3: Relative intensity of the vanadyl petroporphyrin series depending on their double bond equivalent (DBE) in the studied feed fuel and PM samples (no petroporphyrins detected in Particles A).

3.3. Molecular maps as a tool for molecular characterization. Taking advantage of the molecular attributions, DBE versus carbon number diagrams (DBE vs #C) were plotted and used for fingerprint representation. In general, these molecular maps allow for the visualization of alkylated series (horizontal lines) and an easier in-depth comparison between samples. Figure 4 shows the DBE vs #C maps for vanadyl ($C_xH_yN_4VO$) and nickel ($C_xH_yN_4Ni$) porphyrins in both fuels and PM. In the most complex sample, i.e., HFO C, we were able to identify 290 different vanadyl porphyrins and 168 nickel porphyrins. In the most complex PM, we attributed 182 unique vanadyl porphyrins and 97 nickel porphyrins. To the best of our knowledge, it is the first time that these many porphyrins were found in this kind of ultra-complex aerosol matrix.

Vanadyl porphyrins in the fuels sample involved abundant alkylated series at DBE 17, 18 and 20, following the DBE pattern found in Figure 3. For HFO A and B, the maximum value of DBE was lower than for HFO C (24 versus 27), which might be caused by the overall lower relative abundance. Even though nickel porphyrins were detected with significantly lower abundance, they followed the same DBE pattern as the vanadyl analogous. Also, the highest DBE value for Ni porphyrin (max DBE: 26) was just under the maximum value of VO porphyrins (max DBE: 27). The most abundant species of these series were found between carbon number 25 and 30, i.e., close to the PAH planar limit defined by Cho et al[49]. This localization in the DBE versus #C maps implies moderatly alkylated porphyrins.

Porphyrins being among the PAH family, one may expect they would be affected by the combustion by similar transformations. A possible chemical transformation of PAH. during combustion is the dealkylation[13, 28, 50, 51]. Indeed, in the combustion process, side chains can be cleaved off prior to further chemical transformation like, for example, ring opening or oxidation. Another chemical transformation involves formation of PAH from ethyne at high temperature, i.e. by pyrogenesis. Porphyrins, however cannot be generated from smaller building blocks.[28] The comparison between the DBE vs #C of the fuel and particles samples aims to determine if dealkylation or other reaction pathways, such as ring-opening or partial oxidation, take place.

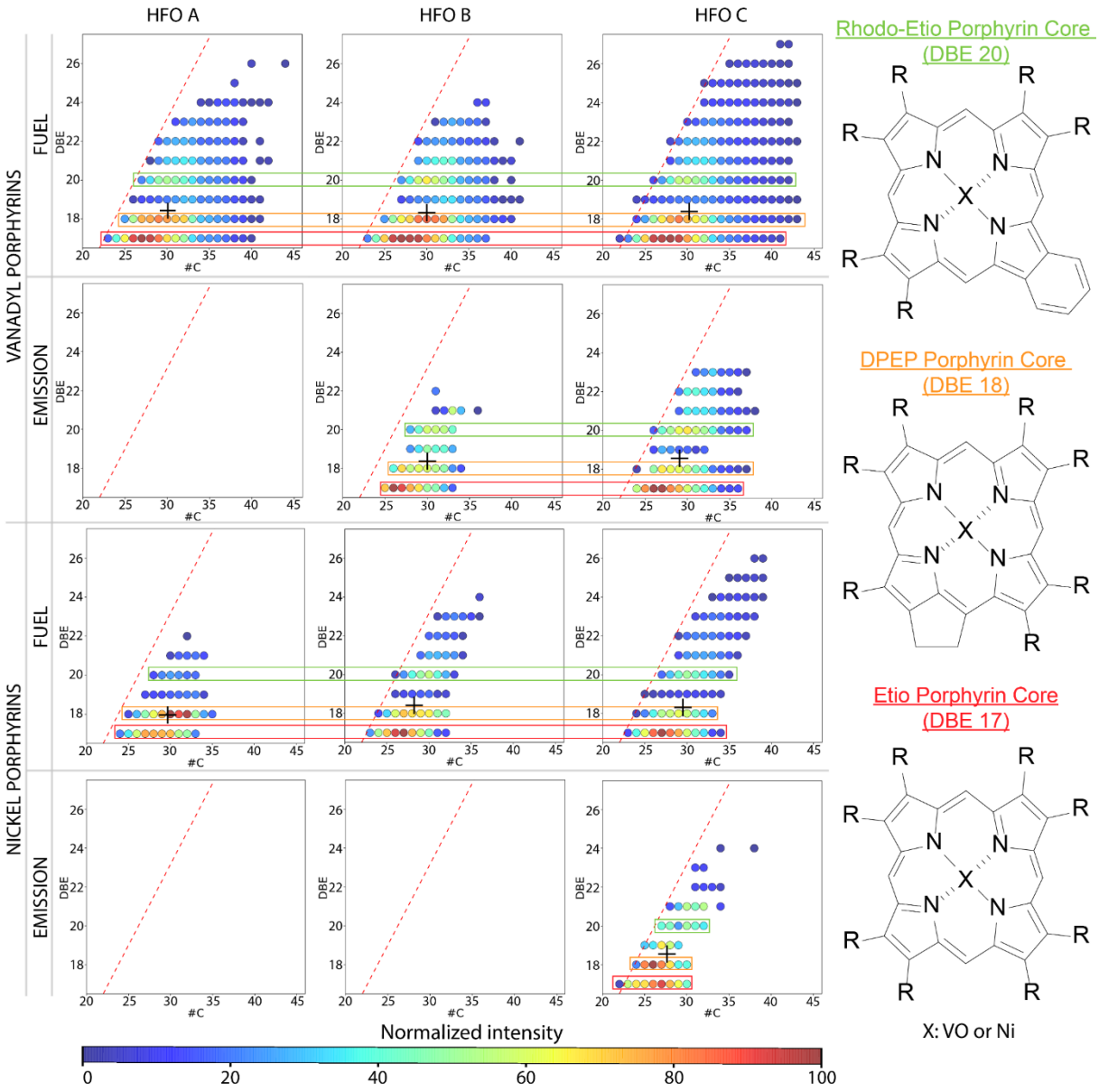

Figure 4: DBE vs carbon number diagrams for vanadyl and nickel porphyrins found in the feed fuels and corresponding primary ship diesel particulate matter samples. The proposed core structures for the main alkylated series are given on the right side and based on fossil petrochemical literature [47]. The planar aromatic limit [49]is given as dashed red line. No vanadyl porphyrins were found for the particulate matter of the HFO A feed and no nickel porphyrins for the particulate matter of the HFO A and B. The center of gravity of the DBE vs #C maps, represented by a black cross, corresponds to an intensity-weighted mean value of DBE and #C.

In the primary emission PM samples, a lower number of species could be detected because of the lower total intensity of the porphyrins fraction, *i.e.* the summed intensity of every porphyrin signals. Indeed, many alkylated species in the series were not detected in the PM, both for vanadyl and nickel porphyrins. We calculated a center of gravity for each DBE vs #C distribution using intensity-weighted values (represented by black crosses in Figure 4). We did not observe any shift of this center

before and after combustion, which suggests that the petroporphyrins were not specifically de-alkylated during the combustion process but uniformly degraded. No DBE homologue rows and, thus, no structures appeared particurlaly targeted by the combustion process. In addition, the same DBE pattern in the feed fuel and PM was observed, supporting the fact that no specific consumption based on the core structure occured during the initial steps of the combustion process and that porphyrins in the particulate matter are essentially a fraction of unburnt fuel. No porphyrins were formed from higher DBE species (by, for example, the ring-opening of an attached benzene group). A putative structure for each most intense value of DBE are given in the Figure 4. These structures are based on previous work[47]. More hypothetical structures are represented in Figure S 5.

The absence of nickel porphyrins in PM B, was most likely due to the low S/N ratio that did not allow for the detection of species with a very low intensity. Indeed, in PM B, the vanadyl porphyrins fraction only accounted for a rather low fraction of 0.55% of the summed intensity of all attributed species, or total intensity. As vanadyl prorphyrins were usually more abundant than the nickel porphyrins, their fraction of the total intensity was expected to be lower, thereby underneath the detection limit. For PM A, the fact that no porphyrins were detected could also be caused by other combustion characteristics, e.g., more efficient combustion with lower emission of unburned species of HFO A , consequently emitting less vanadium and nickel on the particulate matter, as shown in Table 1. Assuming in a first approximation a uniform combustion behavior, this would lead to drastically lower petroporphyrin fractions in the particulate matter. Indeed, the PM emission of the ship diesel engine fed with HFO A is lower in terms of mass concentration as well as in number concentration of particles in the exhaust, independantly of the used engine load.

3.4. Porphyrins fate through the combustion process. Aiming to analyze the combustion pattern, we used the respective fold change normalized to the overall signal yield (summed intensity of all attributed species) to compare HFO C and PM C. For all porphyrins detected in both feed fuel and PM, the fold change value was calculated from peak intensities as follow:

$$FC = \frac{Peak\ intensity\ in\ PM}{Peak\ intensity\ in\ feed\ fuel}$$

In agreement with petroinformatics largely described by Hur et al.[52], the binary logarithm of the FC ($\log_2$[FC]) was then used for color-coding the DBE vs #C maps (Figure 5).

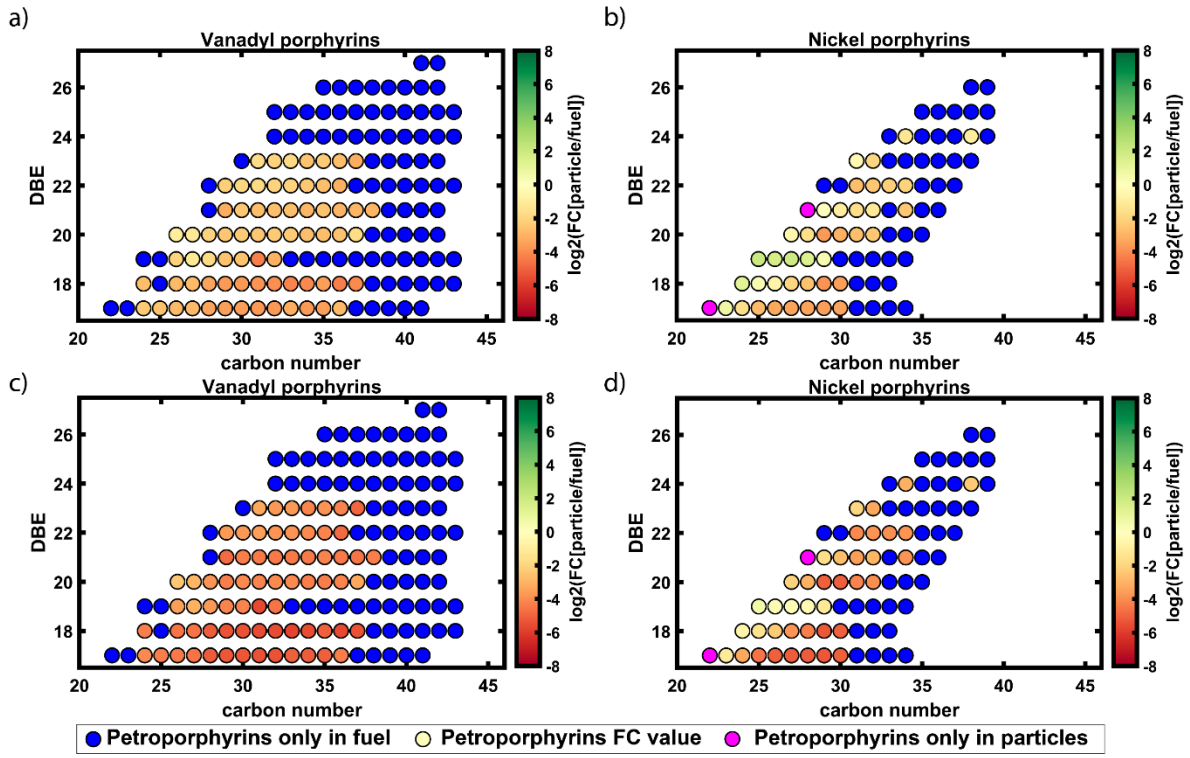

Figure 5: DBE vs #C plot using the log_2[FC] values as color code, highlighting the chemical fate of petroporphyrins through the combustion process in the ship diesel engine. a) Vanadyl porphyrins, intensity relative to the total intensity of identified species, b) Nickel porphyrins, intensity relative to the total intensity of identified species, c) Vanadyl porphyrins, absolute intensity, d) Nickell porphyrins, absolute intensity.

A diagram representing the data treatment strategy for Figure 5 is found in the supporting information (Figure S6). All detected porphyrins are represented: fuel-exclusive and particles-exclusive petroporphyrins are represented by fixed blue and pink colors, respectively. With this approach, the higher the modulus of a log_2[FC] value, the higher the difference between feed fuel and primary emission. Positive values are linked to an increased abundance in the particles, which can only be caused by pyrogenesis or transformation of larger species in smaller constituents, e.g., due to dealkylation or ring-opening reactions. Negative values are caused by a larger abundance in the feed fuel, i.e., consumption and decomposition of the respective petroporphyrin during the combustion process. Additionally, if a log_2[FC] value is close to zero, it means that the represented species is as intense in the fuel as in the particles and no considerable transformation can be assumed or consumption and transformation processes compensate for each other. Figure 5a and 5c present the results for the vanadyl porphyrins; numerous highly-alkylated and -aromatic vanadyl porphyrins were not detected in the particulate matter sample and, thus, are represented as blue dots. Nevertheless, the homogeneity of the FC values demonstrates that no specific combustion process was observed at this molecular level, in agreement with the more general observations for the grouped DBE classes and overall abundance of vanadyl petroporphyrins. Indeed, the fold change values being uniformly distributed under 0 without particles-exclusive porphyrins hints a general consumption with no apparent structural dependence. However, the Figure 5b and 5d representing the nickel porphyrins show that the fold change values vary from negative to positive at

DBE 17 to 19 as the carbon number decreases. This observation could be correlated to a dealkylation process but as the overall intensity of nickel porphyrins is low (under 1% of the total intensity of attributed species in the richest sample), we are unable to affirm this behavior yet. Figure 5a and 5b show the results with the intensities relative to the total intensity of identified species, as opposed to Figure 5c and 5d that use absolute intensities. Each method has its advantages and drawbacks: normalized intensities allow for a homogeneous order of magnitude for the compared values; but, if a species is heavily consumed through combustion, it will increase the relative abundance of all other species in the particles samples, possibly leading to "false" positive fold change values. On the other hand, using absolute intensities palliates this issue but is sensitive to the difference in order of magnitude between the intensities before and after combustion. Hence this second method is limited by the facts that the MALDI method used is here purely qualitative and that it is not possible to correct the difference using the particulate matter mass on the filter and the amount of fuel used in the extraction process.

3.5. Effect of the engine's power load on porphyrins in PM. Particulate matter was obtained by burning HFO C with a motor load of 75 %, reflecting the more optimized condition used in open-sea long-range transport (i.e. cruise state): PM C'. No petroporphyrins were found in this sample (Figure 6). In previous data, where petroporphyrins could be detected well above the S/N-limit, PM samples were generated with 25% load, corresponding to the power load while maneuvering actions or idling in the harbor, The presence of abundant porphyrins can largely be related to the overall lower combustion efficiency with a 25% power load, as the engine is optimized for the 75% load conditions. Even though the PM emissions with 75% load condition account for the longest distances in open-sea transport, the PM that result from the 25% load is emitted closer to the coastal line or directly in the harbor area and are thus expected to have a stronger influence on local and semi-local environmental health. Figure 6 shows the mass spectra of PM C and PM C' at *m/z* 487 where the most intense vanadyl porphyrin ($C_{28}H_{28}N_4OV$, *m/z* 487.16969) is expected.

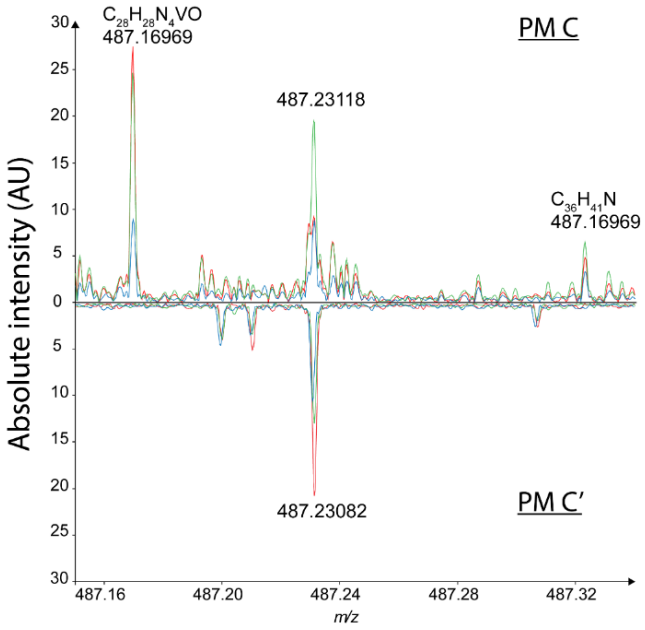

Figure 6: ET-MALDI FT-ICR mass spectra at m/z 487 (350 mDa excerpt) of PM samples obtained from the HFO C feed fuel at different power loads: Up) 25% load (20 kW) harbor maneuvering, , and Down) 75% load (60 kW) cruise long-range. Each color corresponds to an analytical replicate.

Interestingly, even though this usually abundant petroporphyrin appears on the PM C mass spectra, it did not appear on PM C' spectra. The PM C spectra exhibits an important variation in the absolute intensity of the peak of interest (*m/z* 487.16969); nevertheless, the use of the of relative intensities, as partly described in Figure S6, we were able to reduce this variation (See Table S5). The absence of peak above the S/N signal in this region for the mass spectra of PM C' sample suggests that the petroporphyrins present in the fuel are consumed at this load to a point not detectable with the presented ET-MALDI approach;

nevertheless, the limited size of the sample set doesn't allow us to confirm it. The main ion (*m/z* 487.23082) shown in PM C' mass spectra are also found in blank spectrum, so they most likely come from the filter and the matrix used.

4. Conclusion

For the first time, this study allowed to evidence petroporphyrins in primary ship diesel emission at the molecular level by the combination of ultra-high resolution mass spectrometry (FTICR MS) and a selective electron-transfer matrix in ET-MALDI. The α-CNPV-CH3 matrix allowed the characterization of the targeted petroporphyrins because of their highly aromatic character. The evidenced porphyrins consisted of vanadium oxide or nickel complexed inside a tetrapyrrole core, well-known in the fossil feed fuels. These porphyrins were detected, not only in the feed heavy fuel oils, but also in the particles emitted by their combustion under realistic conditions in a one-stroke ship diesel engine.

A general uniform consumption and degradation of the petroporphyrins through the engine combustion was observed with no particular preference for any structural motif, as differentiated by the DBE. Despite the reported effects of a dealkylation on pure PAHs and N/S-PAHs[53], no significant dealkylation effect could be found. Visualized by DBE versus #C maps, an overall reduction of the chemical space after combustion, most likely due to the lower overall abundance, was found. Moreover, the porphyrins in the particulate matter were chemically very close to those of the feed fuel but found in significantly lower abundance. No transformed classes (oxidized, ring-opening) indicated any further combustion fate of the petroporphyrins, known to be very stable. Nonetheless, to confirm this finding, the occurrence of these products will be further studied in future work utilizing novel sampled particulate matter with higher concentration, other combustion conditions, and a bigger sample set. Here also complementary analytical tools, such as APPI and/or positive-ion electrospray ionization-(ESI+) using sodium attachment, can be deployed.

Concerning environmental health, it has been concluded that higher amounts of petroporphyrins might be released by the combustion of heavy fuel oils in harbor areas or close to the coastal line rather than in open sea, based on different engine loading conditions and combustion efficiency. In this respect, the here molecularly proven emission of metal organics is an exciting factor and motivates related health studies. The molecularly resolved and detected emitted petroporphyrin pattern thus add another group of compounds largely unknown to respiratory toxicity. Furthermore, the presence and fate of petroporphyrins in the primary exhaust particulate matter of a ship engine equipped with exhaust gas treatment technology, i.e., scrubber technology and particle filter, motivates future studies. The fate of the highly aromatic and polar petroporphyrins during these washing and removal steps will be of high interest, as trace metals may potentially be introduced directly into the aqueous phase.

Acknowledgments

This work has been partially supported by University of Rouen Normandy, INSA Rouen Normandy, the Centre National de la Recherche Scientifique (CNRS), European Regional Development Fund (ERDF), Labex SynOrg (ANR-11-LABX-0029), Carnot Institut I2C, the graduate school for research Xl-Chem (ANR-18-EURE-0020 XL

CHEM), the European Union's Horizon 2020 Research Infrastructures program (Grant Agreement 731077) and by Region Normandie. We thank the DFG (ZI 764/28-1) and ANR (ANR-20-CE92-0036) for funding of the research project TIMSAC.

References

1. Corbett, J.J., et al., *Mortality from Ship Emissions: A Global Assessment.* Environmental Science & Technology, 2007. **41**(24): p. 8512-8518.

2. Kanashova, T., et al., *Differential proteomic analysis of mouse macrophages exposed to adsorbate-loaded heavy fuel oil derived combustion particles using an automated sample-preparation workflow.* Analytical and Bioanalytical Chemistry, 2015. **407**(20): p. 5965-5976.

3. Corbin, J.C., et al., *Brown and Black Carbon Emitted by a Marine Engine Operated on Heavy Fuel Oil and Distillate Fuels: Optical Properties, Size Distributions, and Emission Factors.* Journal of Geophysical Research: Atmospheres, 2018. **123**(11): p. 6175-6195.

4. Eyring, V., et al., *Transport impacts on atmosphere and climate: Shipping.* Atmospheric Environment, 2010. **44**(37): p. 4735-4771.

5. Czech, H., et al., *A chemometric investigation of aromatic emission profiles from a marine engine in comparison with residential wood combustion and road traffic: Implications for source apportionment inside and outside sulphur emission control areas.* Atmospheric Environment, 2017. **167**: p. 212-222.

6. Agrawal, H., et al., *In-use gaseous and particulate matter emissions from a modern ocean going container vessel.* Atmospheric Environment, 2008. **42**(21): p. 5504-5510.

7. Abadie, L.M., N. Goicoechea, and I. Galarraga, *Adapting the shipping sector to stricter emissions regulations: Fuel switching or installing a scrubber?* Transportation Research Part D: Transport and Environment, 2017. **57**: p. 237-250.

8. Streibel, T., et al., *Aerosol emissions of a ship diesel engine operated with diesel fuel or heavy fuel oil.* Environmental Science and Pollution Research, 2017. **24**(12): p. 10976-10991.

9. Winnes, H. and E. Fridell, *Particle Emissions from Ships: Dependence on Fuel Type.* Journal of the Air & Waste Management Association, 2009. **59**(12): p. 1391-1398.

10. Agrawal, H., et al., *Emission measurements from a crude oil tanker at sea.* Environ Sci Technol, 2008. **42**(19): p. 7098-103.

11. Moldanová, J., et al., *Physical and chemical characterisation of PM emissions from two ships operating in European Emission Control Areas.* Atmospheric Measurement Techniques, 2013. **6**(12): p. 3577-3596.

12. Czech, H., et al., *New directions: Beyond sulphur, vanadium and nickel – About source apportionment of ship emissions in emission control areas.* Atmospheric Environment, 2017. **163**: p. 190-191.

13. Streibel, T., et al., *Aerosol emissions of a ship diesel engine operated with diesel fuel or heavy fuel oil.* Environ Sci Pollut Res Int, 2017. **24**(12): p. 10976-10991.

14. Oeder, S., et al., *Particulate Matter from Both Heavy Fuel Oil and Diesel Fuel Shipping Emissions Show Strong Biological Effects on Human Lung Cells at Realistic and Comparable In Vitro Exposure Conditions.* PLOS ONE, 2015. **10**(6): p. e0126536.

15. Sippula, O., et al., *Particle emissions from a marine engine: chemical composition and aromatic emission profiles under various operating conditions.* Environ Sci Technol, 2014. **48**(19): p. 11721-9.

16. Corbin, J.C., et al., *Trace Metals in Soot and PM2.5 from Heavy-Fuel-Oil Combustion in a Marine Engine.* Environmental Science & Technology, 2018. **52**(11): p. 6714-6722.

17. Caumette, G., et al., *Element speciation analysis of petroleum and related materials.* Journal of Analytical Atomic Spectrometry, 2009. **24**(3): p. 263.

18. Ali, M.F. and S. Abbas, *A review of methods for the demetallization of residual fuel oils.* Fuel Processing Technology, 2006. **87**(7): p. 573-584.

19. Filby Royston H. and V.B.G. J., *Geochemistry of Metal Complexes in Petroleum, Source Rocks, and Coals: An Overview*, in *ACS Symposium Series*. 1987. p. 2-39.

20. Xu, C., et al., *Overlooked Significant Impact of Trace Metals on the Bacterial Community of PM 2.5 in High-Time Resolution.* Journal of Geophysical Research: Atmospheres, 2021. **126**(23).

21. Wang, Y.N., et al., *Temporal dynamics of heavy metal distribution and associated microbial community in ambient aerosols from vanadium smelter.* Science of The Total Environment, 2020. **735**: p. 139360.
22. Reda, A.A., et al., *Gas phase carbonyl compounds in ship emissions: Differences between diesel fuel and heavy fuel oil operation.* Atmospheric Environment, 2015. **112**: p. 370-380.
23. Kleeblatt, J., et al., *Needle trap sampling thermal-desorption resonance enhanced multiphoton ionization time-of-flight mass spectrometry for analysis of marine diesel engine exhaust.* Analytical Methods, 2015. **7**(8): p. 3608-3617.
24. Käfer, U., et al., *Detailed Chemical Characterization of Bunker Fuels by High-Resolution Time-of-Flight Mass Spectrometry Hyphenated to GC × GC and Thermal Analysis.* Energy & Fuels, 2019. **33**(11): p. 10745-10755.
25. Radischat, C., et al., *Real-time analysis of organic compounds in ship engine aerosol emissions using resonance-enhanced multiphoton ionisation and proton transfer mass spectrometry.* Analytical and Bioanalytical Chemistry, 2015. **407**(20): p. 5939-5951.
26. Mueller, L., et al., *Characteristics and temporal evolution of particulate emissions from a ship diesel engine.* Applied Energy, 2015. **155**: p. 204-217.
27. Drewnick, F., et al., *A New Time-of-Flight Aerosol Mass Spectrometer (TOF-AMS)—Instrument Description and First Field Deployment.* Aerosol Science and Technology, 2005. **39**(7): p. 637-658.
28. Rüger, C.P., et al., *Characterisation of ship diesel primary particulate matter at the molecular level by means of ultra-high-resolution mass spectrometry coupled to laser desorption ionisation--comparison of feed fuel, filter extracts and direct particle measurements.* Anal Bioanal Chem, 2015. **407**(20): p. 5923-37.
29. Xu, H., et al., *Characterization of Petroporphyrins Using Ultraviolet−Visible Spectroscopy and Laser Desorption Ionization Time-of-Flight Mass Spectrometry.* Energy & Fuels, 2005. **19**(2): p. 517-524.
30. Rytting, B.M., et al., *Ultrahigh-Purity Vanadyl Petroporphyrins.* Energy & Fuels, 2018. **32**(5): p. 5711-5724.
31. Ryan, D.J. and K. Qian, *Laser-Based Ionization: A Review on the Use of Matrix-Assisted Laser Desorption/Ionization and Laser Desorption/Ionization Mass Spectrometry in Petroleum Research.* Energy & Fuels, 2020. **34**(10): p. 11887-11896.
32. Zhang, Y., et al., *Elucidating the Geometric Substitution of Petroporphyrins by Spectroscopic Analysis and Atomic Force Microscopy Molecular Imaging.* Energy & Fuels, 2019. **33**(7): p. 6088-6097.
33. Giraldo-Dávila, D., et al., *Selective ionization by electron-transfer MALDI-MS of vanadyl porphyrins from crude oils.* Fuel, 2018. **226**: p. 103-111.
34. Ramírez-Pradilla, J.S., C. Blanco-Tirado, and M.Y. Combariza, *Electron-Transfer Ionization of Nanoparticles, Polymers, Porphyrins, and Fullerenes Using Synthetically Tunable α-Cyanophenylenevinylenes as UV MALDI-MS Matrices.* ACS Applied Materials & Interfaces, 2019. **11**(11): p. 10975-10987.
35. Ramírez-Pradilla, J.S., et al., *Comprehensive Petroporphyrin Identification in Crude Oils Using Highly Selective Electron Transfer Reactions in MALDI-FTICR-MS.* Energy & Fuels, 2019. **33**(5): p. 3899-3907.
36. Ramírez-Pradilla, J.S., et al., *Effect of the Ionization Source on the Targeted Analysis of Nickel and Vanadyl Porphyrins in Crude Oil.* Energy & Fuels, 2021. **35**(18): p. 14542-14552.
37. Cho, Y., et al., *Evaluation of Laser Desorption Ionization Coupled to Fourier Transform Ion Cyclotron Resonance Mass Spectrometry To Study Metalloporphyrin Complexes.* Energy & Fuels, 2014. **28**(11): p. 6699-6706.
38. Nyadong, L. and J. Mendez-Arroyo, *Sodium Cationization Electrospray Ionization Orbitrap Mass Spectrometry for Selective Determination of Crude Oil Porphyrins.* Energy & Fuels, 2021.
39. Maillard, J., et al., *Comparison of soluble and insoluble organic matter in analogues of Titan's aerosols.* Earth and Planetary Science Letters, 2018. **495**: p. 185-191.
40. Vetter, W., F.W. McLafferty, and F. Turecek, *Interpretation of mass spectra. Fourth edition (1993). University Science Books, Mill Valley, California.* Biological Mass Spectrometry, 1994. **23**(6): p. 379-379.
41. Müller, W.H., et al., *Dual-polarity SALDI FT-ICR MS imaging and Kendrick mass defect data filtering for lipid analysis.* Analytical and Bioanalytical Chemistry, 2021. **413**(10): p. 2821-2830.
42. McCann, A., et al., *Mass shift in mass spectrometry imaging: comprehensive analysis and practical*

corrective workflow. Analytical and Bioanalytical Chemistry, 2021. **413**(10): p. 2831-2844.
43. Knochenmuss, R., et al., *Secondary ion-molecule reactions in matrix-assisted laser desorption/ionization.* Journal of Mass Spectrometry, 2000. **35**(11): p. 1237-1245.
44. Student, *The Probable Error of a Mean.* Biometrika, 1908. **6**(1): p. 1.
45. Desprez, A., et al., *Study of the Size Distribution of Sulfur, Vanadium, and Nickel Compounds in Four Crude Oils and Their Distillation Cuts by Gel Permeation Chromatography Inductively Coupled Plasma High-Resolution Mass Spectrometry.* Energy & Fuels, 2014. **28**(6): p. 3730-3737.
46. McKenna, A.M., et al., *Advances and Challenges in the Molecular Characterization of Petroporphyrins.* Energy & Fuels, 2021.
47. Maillard, J.F., et al., *Structural analysis of petroporphyrins from asphaltene by trapped ion mobility coupled with Fourier transform ion cyclotron resonance mass spectrometry.* Analyst, 2021. **146**(13): p. 4161-4171.
48. Zhao, X., et al., *New Vanadium Compounds in Venezuela Heavy Crude Oil Detected by Positive-ion Electrospray Ionization Fourier Transform Ion Cyclotron Resonance Mass Spectrometry.* Scientific Reports, 2015. **4**(1).
49. Cho, Y., Y.H. Kim, and S. Kim, *Planar Limit-Assisted Structural Interpretation of Saturates/Aromatics/Resins/Asphaltenes Fractionated Crude Oil Compounds Observed by Fourier Transform Ion Cyclotron Resonance Mass Spectrometry.* Analytical Chemistry, 2011. **83**(15): p. 6068-6073.
50. Saha, M., et al., *Sources of sedimentary PAHs in tropical Asian waters: Differentiation between pyrogenic and petrogenic sources by alkyl homolog abundance.* Marine Pollution Bulletin, 2009. **58**(2): p. 189-200.
51. Yunker, M.B., et al., *PAHs in the Fraser River basin: a critical appraisal of PAH ratios as indicators of PAH source and composition.* Organic Geochemistry, 2002. **33**(4): p. 489-515.
52. Hur, M., S. Kim, and C.S. Hsu, *Petroinformatics*, in *Springer Handbook of Petroleum Technology*, C.S. Hsu and P.R. Robinson, Editors. 2017, Springer International Publishing: Cham. p. 173-198.
53. Rüger, C.P., et al., *Comprehensive chemical comparison of fuel composition and aerosol particles emitted from a ship diesel engine by gas chromatography atmospheric pressure chemical ionisation ultra-high resolution mass spectrometry with improved data processing routines.* Eur J Mass Spectrom (Chichester), 2017. **23**(1): p. 28-39.
54. Virtanen, P., et al., *SciPy 1.0: fundamental algorithms for scientific computing in Python.* Nat Methods, 2020. **17**(3): p. 261-272.

Supporting information

Supporting information contains laser power optimization curves, Kendrick mass defect based extraction, spectrum highlighting the complexity of studied sample, Student's t test and Pearson' correlation results, hypothetical porphyrins core structures and mass spectra suggesting the absence of porphyrins in MGO.

Laser power optimization

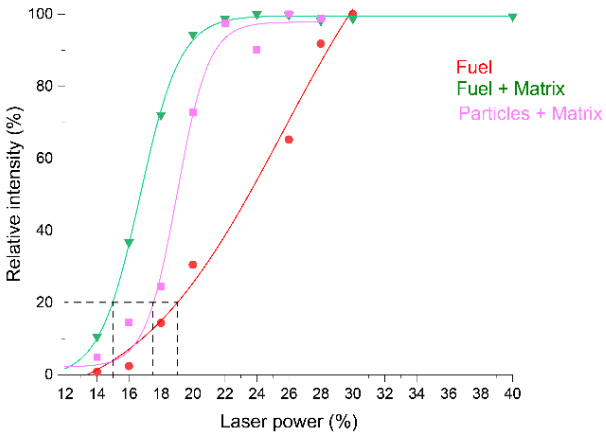

Figure S 1: Laser power optimization curves.

For the three samples displayed in Figure S 1, spectra were recorded at different laser powers (LP) and the total intensity observed was determined, i.e. peak picking was performed with a signal over noise ratio of 4 on the whole spectra and the intensity of every peak was summed. The total intensities for a same sample type were then normalized and plotted against laser power. We chose the laser power corresponding to 20% of the maximum total intensity obtained for each sample type. Laser power had to be optimized in order to obtain a qualitative signal while avoiding the formation of undesired species such as fullerenes.

Engine detail

Engine model	1 VDS 18/15
Method of operation	Four stroke diesel, direct injected, compressor charged
Amount of cylinders	1
Valves	4
Stroke	180 mm
Bore	150 mm
Length of connecting rod	332 mm
Nominal speed	1,500 min^{-1}
Compression ratio	13
Maximum power	80 kW
Nominal power	60 kW

Table S 1: Engine's specifications

This table lists the specifications of the engine used during the measurement campaign which produced our samples. This engine and the running conditions are furthermore detailed by Streiblel et al.[13]

Calibration list

Molecular formula	*m/z* ratio	Molecular formula	*m/z* ratio	Molecular formula	*m/z* ratio
$C_{26}H_{20}$	332.155952	$C_{47}H_{67}N$	645.526803	$C_{26}H_{21}N_2$	361.169925
$C_{27}H_{22}$	346.171602	$C_{48}H_{63}N$	653.495502	$C_{25}H_{20}N_4O_1V_1$	443.107120
$C_{29}H_{24}$	372.187252	$C_{49}H_{65}N$	667.511153	$C_{25}H_{22}N_4O_1V_1$	445.122770
$C_{31}H_{24}$	396.187252	$C_{50}H_{65}N$	679.511153	$C_{26}H_{22}N_4O_1V_1$	457.122770
$C_{33}H_{26}$	422.202902	$C_{50}H_{69}N$	683.542453	$C_{26}H_{24}N_4O_1V_1$	459.138420
$C_{36}H_{30}$	462.234202	$C_{51}H_{63}N$	689.495502	$C_{27}H_{24}N_4O_1V_1$	471.138420
$C_{21}H_{19}N$	285.151201	$C_{50}H_{75}N$	689.589403	$C_{27}H_{26}N_4O_1V_1$	473.154070
$C_{22}H_{17}N$	295.135551	$C_{52}H_{67}N$	705.526803	$C_{28}H_{22}N_4O_1V_1$	481.122770
$C_{23}H_{19}N$	309.151201	$C_{52}H_{73}N$	711.573753	$C_{28}H_{26}N_4O_1V_1$	485.154070
$C_{24}H_{16}N$	318.127726	$C_{52}H_{77}N$	715.605053	$C_{28}H_{28}N_4O_1V_1$	487.169720
$C_{24}H_{25}N$	327.198151	$C_{54}H_{67}N$	729.526803	$C_{29}H_{24}N_4O_1V_1$	495.138420
$C_{26}H_{21}N$	347.166851	$C_{54}H_{77}N$	739.605053	$C_{29}H_{28}N_4O_1V_1$	499.169720
$C_{27}H_{23}N$	361.182501	$C_{55}H_{73}N$	747.573753	$C_{29}H_{30}N_4O_1V_1$	501.185370
$C_{28}H_{25}N$	375.198151	$C_{56}H_{65}N$	751.511153	$C_{30}H_{26}N_4O_1V_1$	509.154070
$C_{29}H_{25}N$	387.198151	$C_{55}H_{79}N$	753.620703	$C_{30}H_{30}N_4O_1V_1$	513.185370
$C_{31}H_{25}N$	411.198151	$C_{57}H_{67}N$	765.526803	$C_{30}H_{32}N_4O_1V_1$	515.201020
$C_{32}H_{27}N$	425.213801	$C_{57}H_{71}N$	769.558103	$C_{31}H_{32}N_4O_1V_1$	527.201020
$C_{40}H_{49}N$	543.385952	$C_{57}H_{79}N$	777.620703	$C_{31}H_{34}N_4O_1V_1$	529.216670
$C_{41}H_{55}N$	561.432902	$C_{57}H_{81}N$	779.636353	$C_{32}H_{34}N_4O_1V_1$	541.216670
$C_{43}H_{51}N$	581.401602	$C_{57}H_{83}N$	781.652003	$C_{33}H_{36}N_4O_1V_1$	555.232320
$C_{44}H_{57}N$	599.448552	$C_{58}H_{79}N$	789.620703	$C_{35}H_{34}N_4O_1V_1$	577.216670
$C_{45}H_{57}N$	611.448552	$C_{59}H_{73}N$	795.573753	$C_{36}H_{32}N_4O_1V_1$	587.201020
$C_{46}H_{57}N$	623.448552	$C_{26}H_{20}N_2$	360.162100	$C_{37}H_{38}N_4O_1V_1$	605.247970
				$C_{39}H_{38}N_4O_1V_1$	629.247970

Table S 2: internal calibration list

This table contains all the ions used to perform the internal calibrations during this study. It is composed of species detected in HFO C such as already known $C_xH_yN_1$ and C_xH_y molecular series and $C_xH_yN_4VO$ species newly identified . Furthermore, two characteristic ions of the matrix were also used: $C_{26}H_{20}N_2$ and $C_{26}H_{21}N_2$.

Kendrick mass defect based extraction

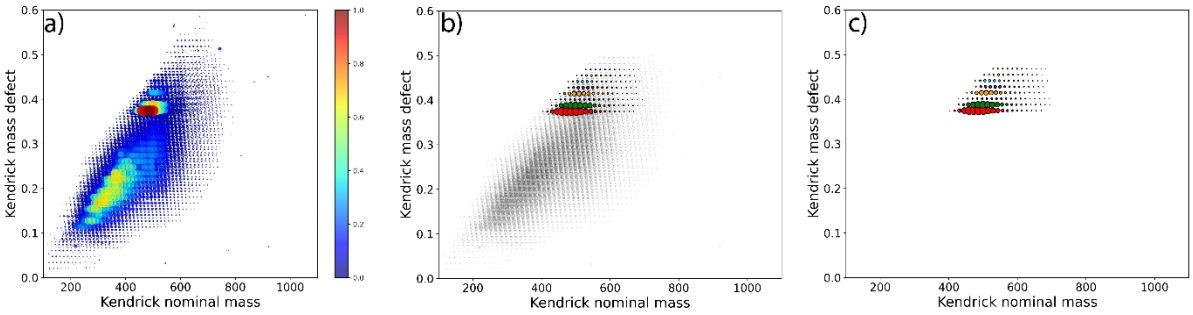

Figure S 2: a) Kendrick's diagram with all species, b) Kendrick's diagram with extracted series stacked on the previous plot, c) Kendrick's diagram with only the extracted series.

The peak picking feature available in Data Analysis 5.0 allowed the Kendrick Mass Defect (KMD) diagram to be plotted (a). Our self-written python routine enables the extraction, both visual and numerical, of selected homologue series. For example, if we enter the *m/z* ratio of $C_{28}H_{28}N_4VO^+$, i.e. *m/z* 487.16972, the program will display a series containing signals with the same KMD, either over the faded global KMD diagram (b) or on a blank diagram (c). The data concerning this specific series, i.e. m/z, intensity, error, etc., can then be extracted to a .csv (comma separated values) file. As seen in Figure S 2) b and c, it is possible to select several series to extract. Then, using this information, we attributed the vanadyl and nickel porphyrins using the following molecular boundaries: $C_xH_yN_4VO_{1\text{-}3}S_{0\text{-}1}$ and $C_xH_yN_4Ni$.

Sample's molecular complexity

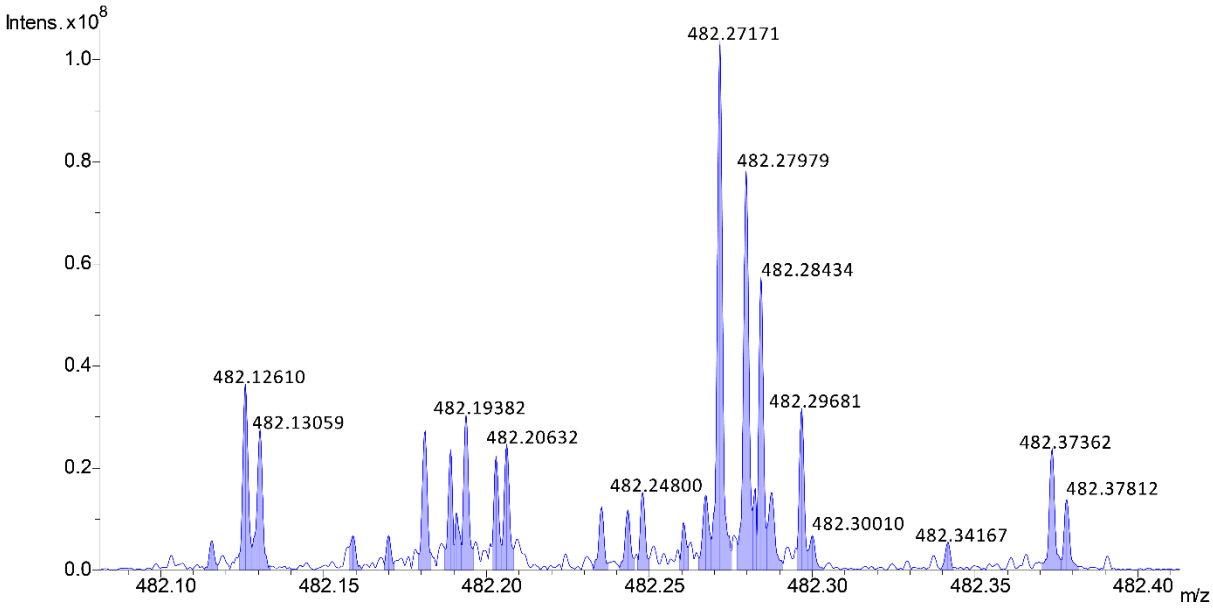

Figure S 3: Sample's molecular complexity

Figure S 3 highlights the complexity of the studied samples. This mass spectrum corresponds to the HFO C sample with the α-CNPV-CH3 matrix and exhibits a total of 26 peaks above the selected S/N ratio (S/N = 4) within the range of 300mDa at *m/z* 482.

Searching for porphyrins in other samples

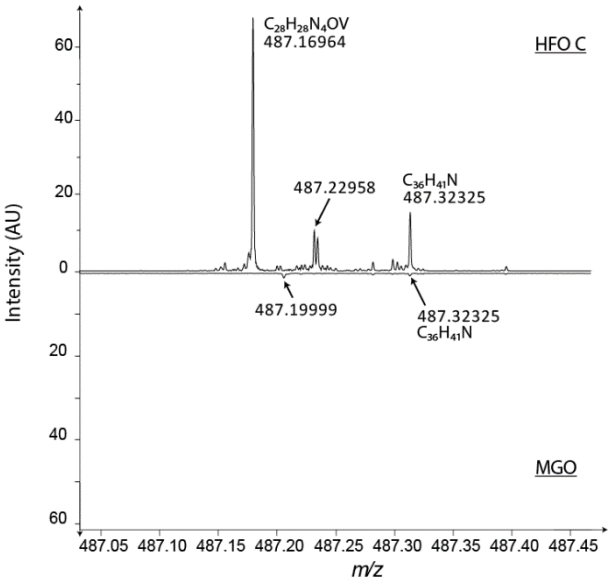

Figure S 4: Two mass spectra zoomed at m/z 487. The upper spectrum corresponds to the HFO C sample and the lower spectrum concerns the MGO sample.

In the mass range displayed in Figure S4, the most intense petroporphyrin found in our main samples, i.e. HFO A, B, C, and Particles A, B, and C, is supposed to be found. However, if we can clearly see it on the HFO C spectrum, this figure demonstrates that this porphyrin isn't found in the MGO sample.

Student's t-test

With the aim of determining if the differences in porphyrins' relative intensity between the samples were significant or not, we realized a Student's t test. We summed the relative intensity of nickel and vanadyl porphyrins for each replicate (3 per sample) and performed the tests on these values. The null hypothesis for these tests is: '*The mean relative intensities of petroporphyrins in the compared samples are equal*' and the chosen alternative hypothesis is '*The mean relative intensities of petroporphyrins in the compared samples are not equal*'. Hence, we realized a two-tailed statistical test as opposed to a one-tailed test whose alternative hypothesis would be: '*The mean relative intensity of petroporphyrins in the studied sample is greater than in the reference sample'*. The t test returns a p value representing the probability that the null hypothesis is true, thus, to be able to affirm that we observe a significant difference between the compared samples with a confidence level of 95%, p must be under 0.05. The p values obtained are shown in table S 1.

Samples compared	p-value
HFO A / HFO B	0.073143
HFO B / HFO C	0.000018
HFO A / HFO C	0.000004
Part. B / Part. C	0.004745
HFO B / Part. B	0.022522
HFO C / Part. C	0.000231

Table S 3: Results of Student's t test

Except between HFO A and B, the observed differences are all significant with a confidence level of 95%.

Pearson's correlation coefficients

The following table contains the Pearson's correlation coefficient obtained by comparing the DBE distribution pattern of fuel samples with the pattern of their corresponding emissions. This comparison was realized under Python using the *scipy[54]* package's "*pearsonr"* function on the mean intensity of each DBE value of the compared samples.

Samples	HFO B/Particles B	HFO C/Particles C
Correlation coefficient	0.9568	0.9771
Significance level α (%)	3.99e-4	2.37e-5

Table S 4: Comparison of DBE distribution patterns using the Pearson correlation coefficient

A correlation coefficient close to 1 exhibits a perfect correlation between the compared datasets, in our case, it would mean that the compared samples have the exact same DBE distribution pattern. However, this only coefficient is not enough to prove similarity. Indeed, we need to be cautious of the significance level (α) which is the probability that the correlation is in fact false. Hence, an α value close to zero is what you look for, even if the commonly accepted maximum α value is 5%.

Porphyrins core

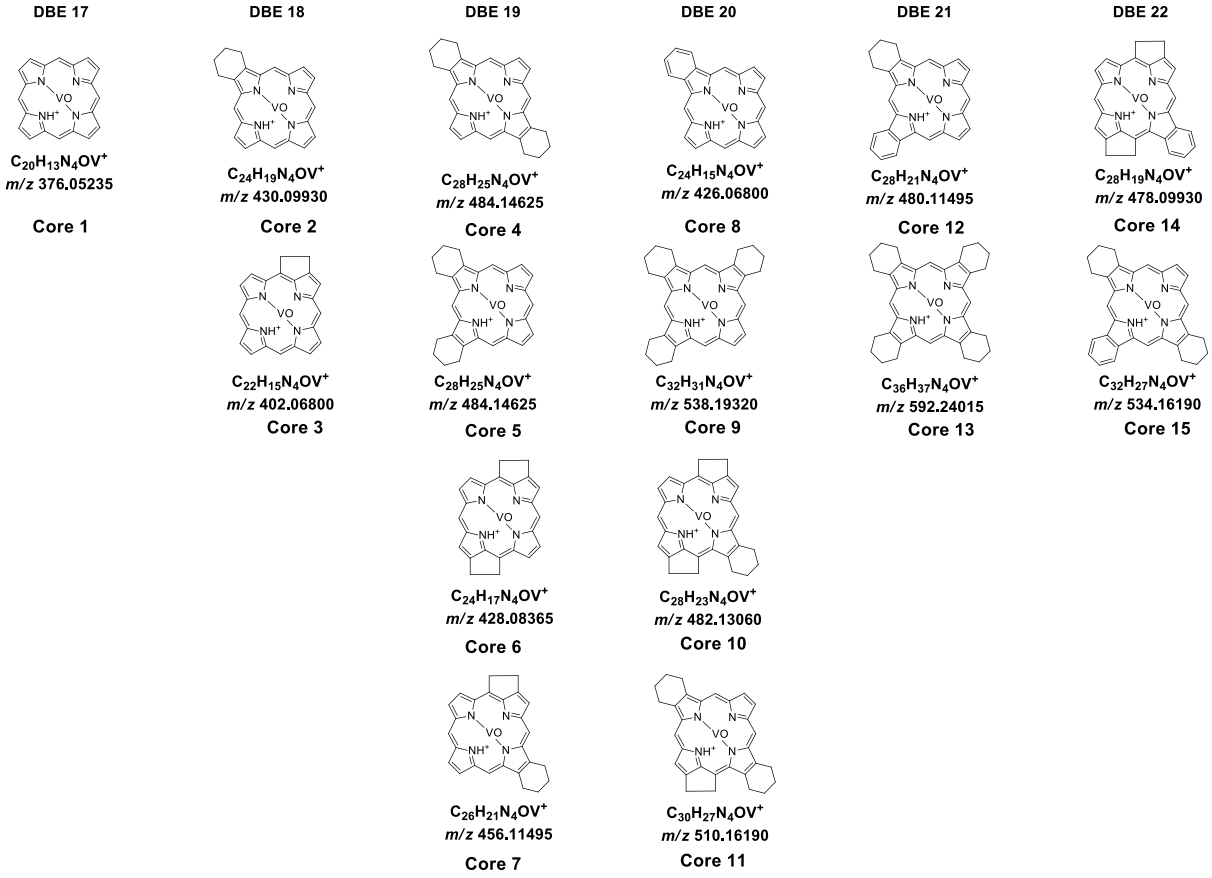

Figure S 5: Possible porphyrin core structures depending on their DBE (Reproduced with the author's agreement[47])

These possible core structures for petroporphyrins were found in previous work by Maillard et al.[47] in which they used trapped ion mobility coupled with Fourier transform ion cyclotron resonance mass spectrometry (TIMS-FTICR MS)

Data treatment workflow

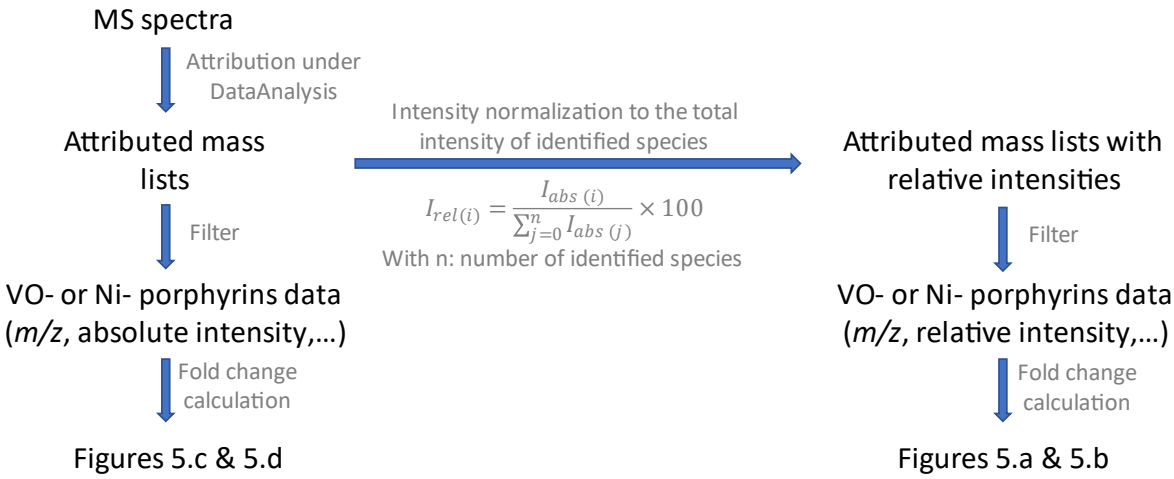

Figure S 6: Data treatment strategy for the establishment of Figure 5

This Figure shows the data treatment strategy used to elaborate Figure 5 and exhibits the difference between Figure 5.a & 5.c and Figure 5.b & 5.d respectively. This difference is the type of intensity chosen to calculate the fold change values. Indeed, the two options have their own advantages and drawbacks, so they both needed to be shown.

Calculation of coefficient of variation

We calculated the coefficient of variation (CV) for both absolute and relative intensities of the peak corresponding to $C_{28}H_{28}N_4OV$ **(***m/z* 487.16969) across the replicates as follows:

$$CV_{abs} = \frac{Standard\ deviation\ of\ abs.intensity}{Mean\ abs.\ intensity} \times 100$$

$$CV_{rel} = \frac{Standard\ deviation\ of\ rel.intensity}{Mean\ rel.\ intensity} \times 100$$

	Absolute intensity	Relative intensity
Coefficient of variation (%)	37.68	20.11

Table S 5: Coefficient of variation values demonstrating the advantage to use relative intensities

References

[1] Streibel T, Schnelle-Kreis J, Czech H, Harndorf H, Jakobi G, Jokiniemi J, et al. Aerosol emissions of a ship diesel engine operated with diesel fuel or heavy fuel oil. Environ Sci Pollut Res Int 2017;24(12):10976-91.

[2] Virtanen P, Gommers R, Oliphant TE, Haberland M, Reddy T, Cournapeau D, et al. SciPy 1.0: fundamental algorithms for scientific computing in Python. Nat Methods 2020;17(3):261-72.

[3] Maillard JF, Le Maitre J, Ruger CP, Ridgeway M, Thompson CJ, Paupy B, et al. Structural analysis of petroporphyrins from asphaltene by trapped ion mobility coupled with Fourier transform ion cyclotron resonance mass spectrometry. Analyst 2021;146(13):4161-71.